Research Article | Vol. 30, No. 9 / 25 Apr 2022 / Optics Express 14828
Optics EXPRESS

Large-area SnTe nanofilm: preparation and its broadband photodetector with ultra-low dark current

LIYUAN SONG,[1,2,3] LIBIN TANG,[1,2,3,5] QUN HAO,[1,6] CHUNLI YANG,[2] KAR SENG TENG,[4,7] HAIPENG WANG,[2] BIAO YUE,[2] JUNBIN LI,[2] AND HONG WEI[2]

[1]*The Laboratory of Photonics Information Technology, Ministry of Industry and Information Technology, School of Optics and Photonics, Beijing Institute of Technology, Beijing 100081, China*
[2]*Kunming Institute of Physics, Kunming 650223, China*
[3]*Yunnan Key Laboratory of Advanced Photoelectronic Materials & Devices, Kunming 650223, China*
[4]*Department of Electronic and Electrical Engineering, Swansea University, Bay Campus, Fabian Way, Swansea SA1 8EN, United Kingdom*
[5]*scitang@163.com*
[6]*qhao@bit.edu.cn*
[7]*k.s.teng@swansea.ac.uk*

Abstract: Photodetectors are receiving increasing attention because of their widely important applications. Therefore, developing broadband high-performance photodetectors using new materials that can function at room temperature has become increasingly important. As a functional material, tin telluride (SnTe), has been widely studied as a thermoelectric material. Furthermore, because of its narrow bandgap, it can be used as a novel infrared photodetector material. In this study, a large-area SnTe nanofilm with controllable thickness was deposited onto a quartz substrate using magnetron sputtering and was used to fabricate a photodetector. The device exhibited a photoelectric response over a broad spectral range of 400-1050 nm. In the near-infrared band of 940 nm, the detectivity (D^*) and responsivity (R) of the photodetector were 3.46×10^{11} cmHz$^{1/2}$w^{-1} and 1.71 A/W, respectively, at an optical power density of 0.2 mWcm^{-2}. As the thickness of the SnTe nanofilm increased, a transition from semiconducting to metallic properties was experimentally observed for the first time. The large-area (2.5cm × 2.5cm) high-performance nanofilms show important potential for application in infrared focal plane array (FPA) detectors.

1. Introduction

Near-infrared (NIR) photodetectors have found many important applications in optical fiber communication, autonomous vehicles (*e.g.*, in range finding, infrared imaging and night vision), biometric recognition system (*e.g.*, using fingerprints, eyes iris and face), optocouplers, and other fields [1,2]. Two-dimensional (2D) materials, such as graphene, transition metal sulfide, perovskite, black phosphorus, and topological insulators, have attracted significant research interest due to their respective advantages in the photodetector fields [3]. For example, topological insulators (TIs) exhibit properties such as highly conductive surface states and narrow bulk band gap which are suitable for NIR photodetectors [4–6]. However, the light absorption ratio of such devices is relatively small, especially in the NIR region, thus limiting device performance.

SnTe, a relatively new material, is a topological crystal insulator (TCI) and has a highly symmetrical crystal structure. Its topological surface states are protected by crystal symmetry (mirror symmetry). The highly symmetrical crystal planes have Dirac electronic states, which are not scattered by impurities. Therefore, SnTe can be used in electronic devices with minimal energy

#454587 https://doi.org/10.1364/OE.454587
Journal © 2022 Received 25 Jan 2022; revised 25 Mar 2022; accepted 29 Mar 2022; published 20 Apr 2022

Optics EXPRESS

consumption. SnTe has potential applications in broad spectrum (UV-Vis-IR) photodetectors because of its gapless topological surface states and narrow bulk band gap. In addition, SnTe-based photodetectors will exhibit ultra-fast responses due to the high hole mobility of SnTe at room temperature [7]. However, the current research on SnTe still mainly focuses on its physical and thermoelectric properties, while studies on SnTe photodetectors are rarely reported. In addition, the preparation of large-area SnTe nanofilms with high-quality still faces considerable challenges, which must be overcome for the fabrication of focal plane array (FPA) detectors.

Over the past years, SnTe based photodetectors have been developed and studied by several groups. For example, Gu et al. [8] prepared a SnTe/Si photovoltaic detector for the first time using the CVD method in 2017. Under 808-nm laser irradiation, the device demonstrated a light response but was limited in the detection wavelength. In the same year, Jiang et al. prepared a photoconductive detector based on ultra-thin 2D single crystal SnTe films [9]. The device exhibited a photoelectric response over a broad wavelength from visible light to mid-infrared (405-3800 nm); however, MBE equipment is expensive. In 2020, Liu et al. [10] prepared an ultra-thin SnTe nanosheet using the CVD method and fabricated a photodetector, which responded over a wide spectral range of 400-1050 nm. Under 980-nm laser irradiation, the device demonstrated a responsivity (R) and detectivity (D^*) of 698 m A·W^{-1} and 3.89×10^8 Jones, respectively. However, the small size of the nanoplates render them unsuitable for use in large-scale focal plane arrays and other multi-pixel detectors. In 2021, Feng et al. [11] prepared infrared photodetectors based on SnTe quantum dots. The device exhibited low dark current at room temperature and achieved a broad spectrum photoelectric response from visible light to the 2 μm band. However, its detection and response rates in the NIR band were relatively low.

In this study, we developed a novel broadband photodetector in which a large-area SnTe nanofilm with controllable thickness was deposited onto a quartz substrate using magnetron sputtering. Without annealing, the sputtered nanofilm has already crystallized, which is economical and efficient for the preparation of photodetectors. The photodetector exhibited a low dark current (-4.3 nA) at a bias voltage of -6.0 V, ensuring the low noise of the photodetector. Under 940 nm illumination, the responsivity (R) and detectivity (D^*) of the photodetector could reach up to 1.71 AW^{-1} and 3.46×10^{11} cmHz$^{1/2}$W^{-1}, respectively, superior than the previously reported. Furthermore, the SnTe photodetector is important for developing a novel FPA detector. For the first time, we experimentally showed the thickness-dependent electrical properties of the SnTe nanofilm transiting from the semiconducting to metallic with increasing film thickness, showing important various applications of SnTe based devices in the future.

2. Experiments

2.1. Preparation of SnTe nanofilms and photodetector

SnTe nanofilms were prepared using a magnetron sputtering technique (SPS-T-S100N-2G). First, the quartz substrate (2.5 cm × 2.5 cm) was cleaned with a mixture of ammonia, hydrogen peroxide, and deionized water (1:1:3) and soaked for 30 min at 80 °C. The substrate was then rinsed with flowing deionized water and dried with high purity nitrogen. Subsequently, the substrate was placed in the magnetron sputtering chamber. A SnTe single target (purity 99.99%, purchased from Zhongnuo Advanced Material Technology Co., Ltd) was used. Once the vacuum reached 7.5×10^{-4} Pa, nanofilms with different thicknesses were prepared by sputtering by controlling the deposition duration without increasing the substrate temperature. An argon flow rate of 80 to 100 sccm was applied. The target sputtering power applied was between 40 and 80 W (RF mode). The gas pressure in the chamber was maintained at 5 Pa. The sputtering durations for samples A, B, C, D, E, F, and G were 5, 10, 20, 120, 360, 420, and 720 s, respectively.

Cr/Au was used as the metal electrode in the SnTe photodetector. The preparation process of the electrodes was as follows: (1) spray coating of photoresistor (ACS200 model), baking (at 80 °C for 15 min on a hotplate), exposure to UV for 14 s, photoresist development for 3 min,

Optics EXPRESS

and baking again (at 80 °C for 10 min). (2) Deposition of metal electrodes using Cr and Au targets once the vacuum reached 1.0×10^{-3} Pa. (3) Removal of metal on the photoresist and the photoresist using acetone. (4) Wire bonding carried out to draw gold wires from the electrodes. The thickness of the gold wire was 25 μm.

X-ray diffraction (XRD) spectroscopy (Empyrean), transmission electron microscopy (TEM) (Tecnai G2 TF30), and Raman Spectroscopy (Invia) were used to analyze the structure and crystallinity of the SnTe nanofilms. The elemental composition and chemical bonding at the nanofilms were characterized by X-ray photoelectron spectroscopy (XPS) (K-Alpha+). The thickness and surface morphology of the nanofilms were studied using AFM (Model Seiko SPA-400). The temperature dependent resistivity of the SnTe nanofilms at different thicknesses was measured using a two-probe method. The Keithley 2400 digital source meter and a temperature controller (Model ZWK-5A) were used for measurements under dark conditions. The nanofilms were encapsulated in a liquid nitrogen metal dewar.

2.2. Characterization of SnTe photodetector

The current–voltage (I–V) measurement on the SnTe photodetector was performed in a dark box at room temperature using a Keithley 2400 digital source meter. LED lights of different wavelengths (*e.g.*, 400, 660, 740, 850, 940, and 1050 nm) were used as illumination sources. The optical power density of the different light wavelengths was measured using an FZ400 optical power meter. Transient response measurements were performed using the Keithley 2400 source meter and DG 1022U waveform signal generator under the illumination of different light wavelengths.

3. Results and discussion

3.1. Preparation of large-area SnTe nanofilms by magnetron sputtering and their structural characterization

The preparation process of large-area SnTe nanofilms by the magnetron sputtering method is illustrated in Fig. 1(a). During sputtering, argon gas (Ar_2) was ionized into argon ions (Ar^+). These high-energy ions were bombarded onto the SnTe target and sputtered particles onto the substrate surface to form a SnTe nanofilm. In the process of magnetron sputtering, nano-films with good crystallinity can be obtained at room temperature and do not need annealing treatment. The face-centered cubic structure of SnTe is shown in Fig. 1(b). This β-SnTe can exist stably at room temperature [12].

The phase and crystallinity of the SnTe nanofilm were studied using XRD. The XRD patterns revealed distinctive peaks at the unannealed SnTe nanofilms deposited at different sputtering powers, as shown in Fig. 1(c). Compared with the standard values of the lattice parameters (*e.g.*, $a = b = c = 6.323$Å, $\alpha = \beta = \gamma = 90°$) in PDF# 46-1210 card for cubical SnTe, the diffraction peaks observed at 2θ values of 28.19°, 40.28°, 49.88°, 58.28 °, 65.97 °, and 73.22 °, which were respectively assigned to the crystal planes of (200), (220), (222), (400), (420), and (422). This is also in good agreement with the results in previous reports [13]. The results showed that the prepared SnTe nanofilms were face-centered cubic ($Fm\bar{3}m$) and only had a single-phase; therefore, the prepared SnTe photodetector was based on this crystal structure. Moreover, both the (200) and (220) planes were dominant planes. With an increase in the sputtering power, the FHWM of the peaks exhibited minimal change, but the intensity of the peaks was increased.

Figure 1(d-g) shows the TEM images of the unannealed SnTe nanofilm. Lattice fringes can be observed covering a large-area in the high-resolution TEM (HRTEM) image, as shown in Fig. 1(f). This indicates that the nanofilm has a high degree of crystallization. The interplanar spacings of lattice fringes from the (200) and (220) planes were 0.316 and 0.224 nm as indicated in purple and blue regions in Fig. 1(g), respectively. These results are consistent with previous

Optics EXPRESS

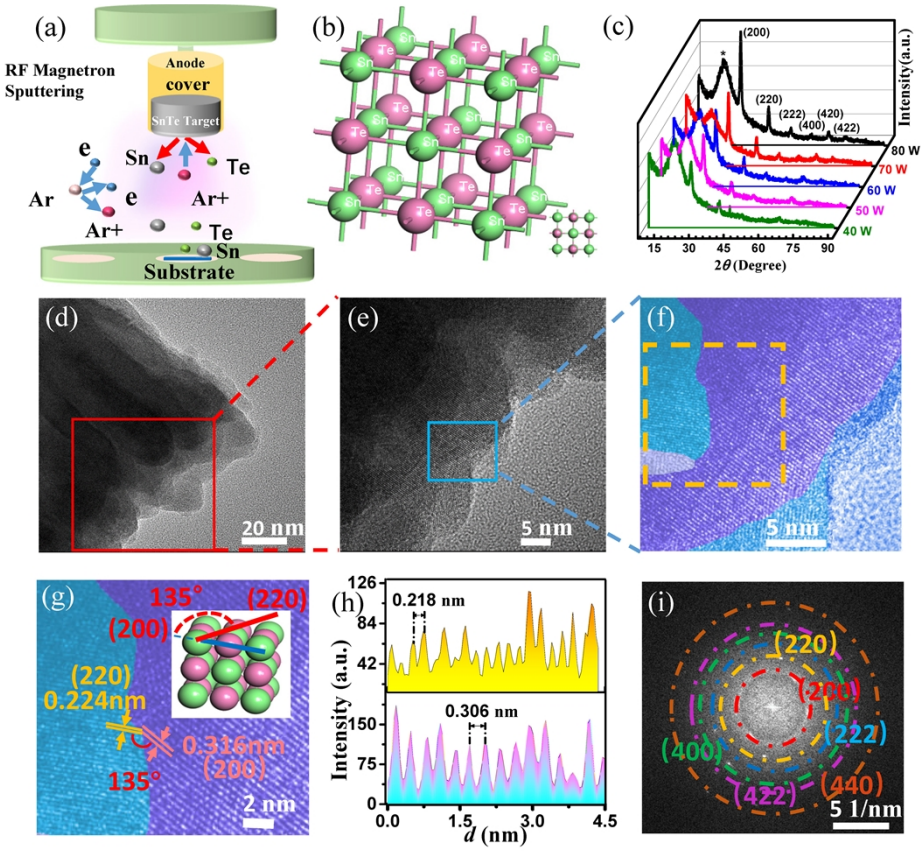

Fig. 1. Preparation and structural characterization of SnTe nanofilms. (a) Schematic diagram depicting the deposition of SnTe nanofilm by magnetron sputtering method. (b) Schematic diagram illustrating the structure of face-centered cubic crystals. (c) XRD spectra of SnTe nanofilms sputtered at different sputtering powers. (d-e) Low resolution TEM images of SnTe nanofilms. (f-g) High resolution TEM images of SnTe nanofilm (Inset: Schematic diagram of the crystal structure). (h) Line profiles showing the interplanar spacings in Fig. (g). (i) Fast Fourier transform (FFT) image of the SnTe nanofilm.

Optics EXPRESS

reports [10]. In addition, the measured angle was 135° between the (200) and (220) planes, as depicted in the inset of Fig. 1(g). The observed (200) and (220) planes in the HRTEM image also corresponded to the first and second strong peaks in the XRD patterns. Figure 1(h) shows the line profiles of the interplanar spacings in Fig. 1(g). The fast Fourier transform image of the SnTe nanofilm is shown in Fig. 1(i). The spot-like diffraction patterns indicated that the prepared SnTe nanofilm was polycrystalline and also corresponded to the different planes revealed in the XRD patterns. The results did not show the presence of other phases or substances, which suggests that the large-area SnTe nanofilm with high-quality was prepared by magnetron sputtering.

3.2. Morphology, crystal structure, and chemical bonding characterizations of SnTe nanofilms with different thicknesses

AFM was performed to characterize the thickness of the SnTe nanofilms and its surface morphology. Figure 2(a) and (b) show the film thickness and root-mean-square (*RMS*) surface roughness of 100 nm and 3.8 nm, respectively, for a sputtering duration of 360 s. When sputtered for a duration of 5 s, the film thickness and *RMS* surface roughness were 4.5 nm and 0.4 nm as shown in Fig. 2 (c) and (d), respectively. The surfaces of the prepared large-area nanofilms were uniform and continuous. Compared with the thicker nanofilm (100 nm), the ultra-thin nanofilm (4.5 nm) has a smaller *RMS* surface roughness, which provided a much better contact with metal electrodes during the fabrication of the photodetectors.

The crystal structures of the nanofilms were further characterized by Raman spectroscopy with an argon-ion laser at an excitation wavelength of 514 nm. As shown in Fig. 2(e), the ultra-thin SnTe nanofilm, with a thickness of 4.5 nm, showed two representative Raman peaks at 122.7 and 140.1 cm^{-1}. The results are consistent with those reported in previous work [10,14], which further implies the high quality of ultra-thin SnTe nanofilms prepared by magnetron sputtering. However, when compared with bulk SnTe [15], these Raman peaks were red-shifted by several wave numbers, which may be due to the quantum size effect of the 2D nanofilm [14]. As for the thicker film with a thickness of 100 nm, the two representative Raman peaks appeared at 120.2 and 140.0 cm^{-1}, and the intensity of the peaks was weaker than those from the ultra-thin SnTe nanofilm. Figure 2(f) illustrates the Raman vibration modes [16]. Raman peak at 122.7 and 140.1 cm^{-1} for ultra-thin SnTe nanofilms were attributed to the characteristic A1 (optical phonon) and ETO (transverse optical phonon) vibration modes, respectively.

The elemental composition and chemical bond of the SnTe nanofilm were studied by XPS using a monochromatic Al Kα source with an energy of 1486.6 eV. Both $3d_{5/2}$ and $3d_{3/2}$ of Te 3d and Sn 3d core levels had been collected here. Figure 2(g) and (h) show the XPS spectra of Te 3d and Sn 3d core level peaks of the 100 nm thick SnTe nanofilm. The Sn $3d_{5/2}$ peak was deconvoluted into three components—SnTe, SnO, and SnO_2—at binding energies of 485.08, 486.18, and 486.98 eV, respectively. The Te $3d_{5/2}$ peak was deconvoluted into two components—SnTe and Te—at 572.08 and 573.88 eV, respectively. These results are consistent with the results of previous reports [17,18]. Since XRD and TEM results did not show any sign of Sn and Te oxides, the oxides in the XPS results were possibly caused by surface oxidation at the SnTe nanofilm during storage and transfer. Figure 2(i) and (j) show the Sn 3d and Te 3d core level peaks of ultra-thin SnTe nanofilms with a thickness of 4.5 nm. Compared with the 100-nm thick nanofilm, the Te $3d_{5/2}$ peak was deconvoluted into three components instead of two. An extra component associated with TeO_3 was positioned at 576.18 eV with a relatively small proportion of 4.86%. The proportion of Sn-O bonds (*e.g.*, SnO and SnO_2) in the Sn $3d_{5/2}$ core level peak of the 4.5 nm thick nanofilm was smaller than that of the 100 nm thick nanofilm. The smaller proportion may be due to the smaller *RMS* surface roughness of the ultra-thin nanofilm, which resulted in a smaller degree of Sn oxidation at the surface. In addition, surface Sn atoms would oxidize more easily than surface Te atoms in both nanofilms. The XPS results also highlighted the presence of elemental Te (Te metallic state) in both nanofilms. This could be caused by Sn vacancies,

Optics EXPRESS

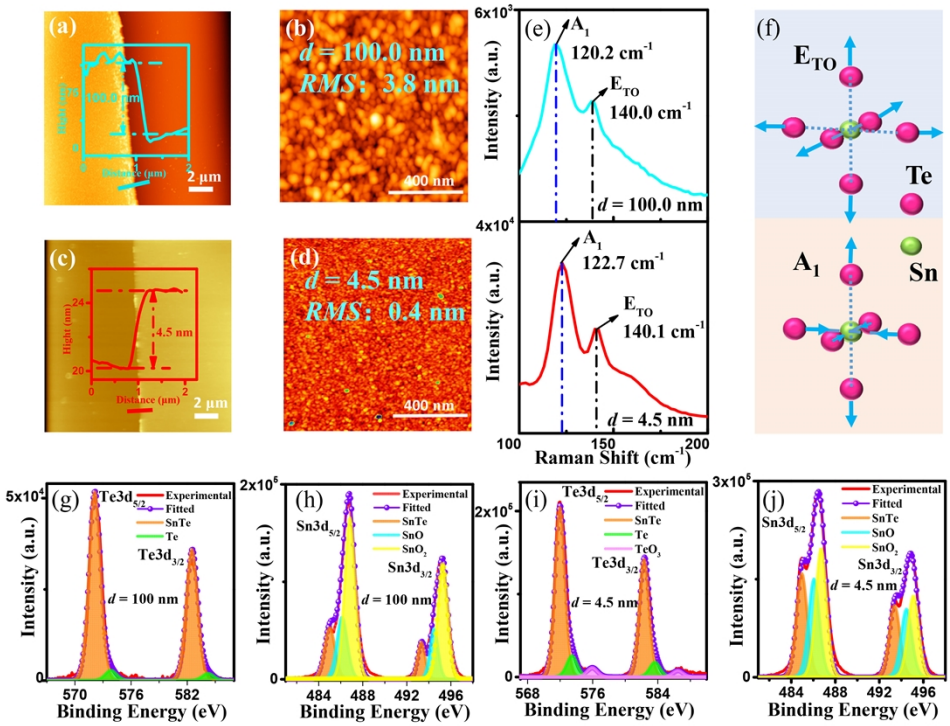

Fig. 2. Morphology, crystal structure, and chemical bonding characterizations of SnTe nanofilms with different thicknesses. (a-d) AFM images on step edges of 100- and 4.5-nm thick nanofilms are shown in (a) and (c), respectively (Inset: Line profiles for thickness measurements). AFM images of SnTe nanofilms with *RMS* roughness measurements for both nanofilms thicknesses are shown in (b) and (d). (e) Raman spectra of SnTe nanofilms with thicknesses of 100 and 4.5 nm. (f) Schematic diagram of Raman vibration modes [16]. (g-j) XPS patterns of Te 3d and Sn 3d core levels of SnTe nanofilms with thicknesses of 100 and 4.5 nm.

which could lead to the neighboring Te atoms having non-bonding orbitals and resulting in the Te metallic state with higher binding energy [17].

3.3. *Thickness dependent ρ-T of SnTe nanofilms*

The resistivity of SnTe nanofilms with different thicknesses was measured at various temperatures. Figure 3(a) shows the temperature dependent resistivity plot of the SnTe ultra-thin nanofilm with a thickness of 4.5 nm (sample A). As the temperature increases, the resistivity showed an overall decreasing trend in the temperature range of 77–273 K, thus exhibiting semiconducting properties. According to the literature [15], the perturbation observed at ~115 K could be due to the structural phase transition from the cubic structure ($Fm\bar{3}m$) to the ferroelectric rhombohedral structure ($R\bar{3}m$) because of a reduction in temperature. Figure 3(b) shows a resistivity plot of sample C with a film thickness of 7.5 nm, and the resistivity of the thicker nanofilms was five orders of magnitude smaller than that of sample A. The resistivity plot of the 100 nm thick nanofilm (sample F) is shown in Fig. 3(c), which revealed increasing resistivity as the temperature increased, thus exhibiting metallic property [19–21]. Figure 3 (d) shows the resistivity values for various film thicknesses at room temperature (300 K). The resistivity of the nanofilm decreased as the thickness of the film increased. For example, the resistivity of sample A was 7×10^{2} Ωcm and decreased sharply to 2.93×10^{-4} Ωcm for sample C with an increased nanofilm thickness.

Optics EXPRESS

In 2015, using first-principles calculations, Qian et al. [22] proved that the bandgap of SnTe nanofilms can be regulated by controlling the film thickness; thus, the films can be transformed from semiconductor to metal. Because SnTe is a topological crystal insulator (TCI), the surface states have an important effect on the structure of SnTe nanofilms. When the nanofilm thickness changes, the structure of SnTe nanofilms may change. There may be a critical thickness that causes structural changes in SnTe nanofilms. When the film thickness reduces, the SnTe nanofilm is significantly affected by the surface states and exhibits semiconductor properties. When the film thickness exceeds a certain value, it becomes less affected by the surface states and presents metallic properties. Such transition was observed experimentally in this work for the first time. Figure 3(e) illustrates the energy band diagrams of SnTe nanofilms with varied film thicknesses. When the thickness of the nanofilm was ≥21.6 nm (sample D), the material presented metallic properties. As the thickness of the nanofilm decreased to ~7.5 nm (sample C), the material was probably in the metal–semiconductor transitional state. However, when the thickness of the nanofilm was reduced to ~5.8 nm (sample B), the material exhibited semiconductor properties.

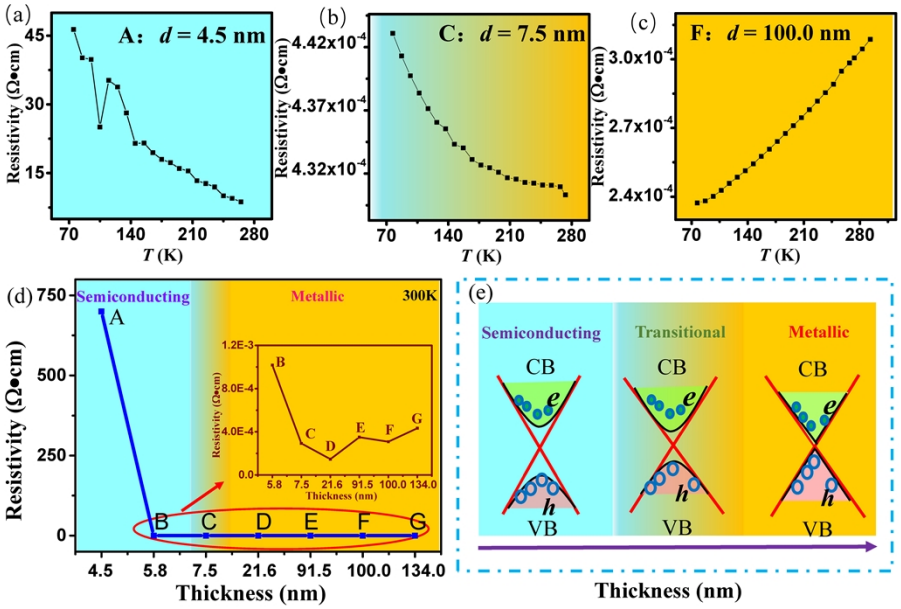

Fig. 3. Temperature dependent resistivity plots (ρ-T) of SnTe nanofilms with different thicknesses. (a-c) ρ-T plots of SnTe nanofilms with different thicknesses of 4.5, 7.5, and 100 nm in the temperature range of 77–273 K. (d) Resistivity (at 300 K) plotted against the thickness of the nanofilms (Inset: Enlarged view on part of the plot). Sputtering durations of samples A, B, C, D, E, F, and G were 5, 10, 20, 120, 360, 420, and 720 s, respectively. (e) Schematic diagram illustrating the changes in the energy band of SnTe nanofilms at different thicknesses.

3.4. *Photodetector performance based on an ultra-thin SnTe nanofilm*

A prototype photodetector based on an ultra-thin SnTe nanofilm (with thickness of 4.5 nm) was fabricated on a quartz substrate. Figure 4(a) illustrates the fabrication process of the device. We performed *I-V* measurements to evaluate the photoelectric response of the device under different light wavelengths, as shown in Fig. 4(b). The plot shows that the photodetector significantly responded to the near-infrared band (*e.g.*, 1050, 940, 850 and 740 nm) as well as the visible light band (*e.g.*, 400 and 660 nm).

Optics EXPRESS

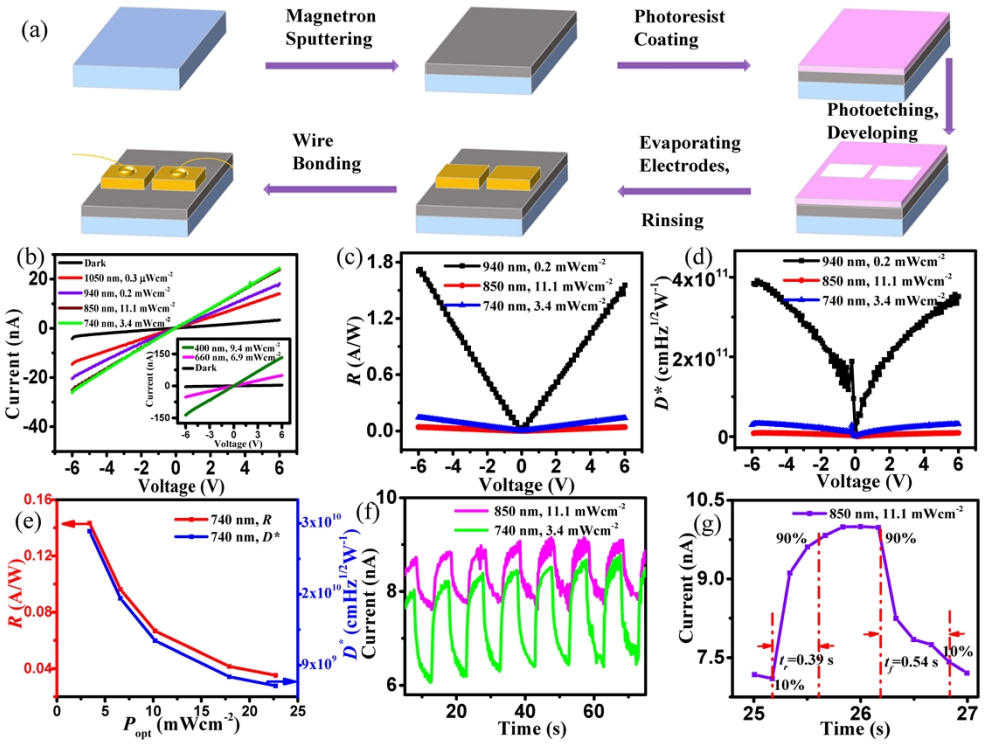

Fig. 4. Characterization of the photodetector based on an ultra-thin SnTe nanofilm. (a) Schematic diagram illustrating the fabrication process of the photodetector. (b) *I*–*V* plots of the photodetector under dark (black line) and varying light illumination. (c) Plot of responsivity (*R*) against *V* under varying NIR illumination of 740, 850, and 940 nm at a voltage bias of -6.0 V. (d) Plots of detectivity (*D**) against *V* under varying NIR illumination of 740, 850, and 940 nm at a voltage bias of -6.0 V. (e) Plot of responsivity (*R*) and detectivity (*D**) against optical power density under an illumination of 740 nm at a voltage bias of -6.0 V. (f) Photocurrent switching behavior of the device at a voltage bias of -6.0 V under 740 and 850 nm illumination. (g) An enlarged view of the light response, including the rising and falling characteristics, of the photodetector.

Optics EXPRESS

The performance of the photodetector is usually characterized by responsivity (R) and detectivity (D^*), which can be defined using the following formula [23]:

$$R = J_{ph}/P_{opt} \tag{1}$$

$$D^* = \frac{R}{\sqrt{2q|J_{dark}|}} \tag{2}$$

where J_{ph} is the photocurrent density, $P_{opt}$is the incident optical power, q is the unit charge, and J_{dark} is the dark current density. The current density (J) is the ratio of the current (I) to the effective photosensitive area (A) of the device:

$$J = I/A \tag{3}$$

The responsivity (R) and detectivity (D^*) of the photodetector could reach up to 1.71 AW^{-1} and 3.46×10^{11} $cmHz^{1/2}W^{-1}$, as shown in Fig. 4(c) and (d), respectively, under 940 nm illumination with an optical power density of 0.2 $mWcm^{-2}$ under a voltage bias of -6 V. The photosensitive area of the device was 4.5×10^{-5} cm^2. The performance of the device at NIR band was significantly better than those previously reported for SnTe-based photodetectors [10,11]. This was probably due to the low dark current (-4.3 nA) at a biased voltage of -6.0 V.

The responsivity and detectivity of the device at different optical power densities are represented by red and blue lines, respectively, in Fig. 4(e). Under 740 nm illumination, both responsivity and detectivity decreased with an increase in optical power density, which was consistent with previously reported results [8,26].

The transient response (I–T) characteristics of the device in the NIR band are shown in Fig. 4(f) and (g). Under 850 nm illumination, the measured rise and fall time were 0.39 and 0.54 s, respectively. Although the response rate was slower than those of SnTe-based photovoltaic devices [8,24,25], it was better than those of reported photoconductive devices [10,11].

The performances of TI and TCI based photodetectors using Bi_2Te_3, Sb_2Te_3, $Pb_{1-x}Sn_xSe$ and SnTe are listed in Table 1. As compared to previous works, the device reported in this work demonstrated relatively good performances. Furthermore, its performance remained stable even after six months.

Table 1. Performance comparison of the photodetectors based on TI and TCI materials

Materials	Devices	Wavelength/nm	R/($A\cdot W^{-1}$)	D^*/Jones	Ref.
$SnTe/SiO_2$	Photoconductor	400-1050	1.71 (940 nm)	3.46×10^{11} (940 nm)	This work
SnTe/mica	Photoconductor	980	6.98×10^{-1}	3.89×10^{8}	[10]
SnTe quantum dots	Photoconductor	2000	3.70×10^{-3}	1.30×10^{9}	[11]
$SnTe/Bi_2Se_3$	Photovoltaic detector	1550	1.46×10^{-1}	1.15×10^{10}	[25]
Bi_2Te_3 nanoplate	Photodetector	850	5.06×10^{-2}	5.92×10^{7}	[26]
SnTe/Si	Photovoltaic detector	254-1550	1.28×10^{-1}	8.40×10^{12}	[8]
$Pb_{1-x}Sn_xSe$	Mid-Infrared detector	1900-2000	3.18×10^{-1}	1.14×10^{12}	[27]
Sb_2Te_3/STO	Photovoltaic detector	405-1550	4.80×10^{-3}	8.60×10^{10}	[5]

Optics EXPRESS

4. Conclusions

We prepared high quality, large-area SnTe nanofilms with controllable thicknesses by magnetron sputtering. The as-prepared SnTe nanofilms were already crystallized without annealing treatment. The manufacturing process was highly efficient and required low energy consumption. The thickness-dependent electrical properties of the SnTe nanofilm transiting from the semiconducting to metallic states with increasing film thickness were experimentally observed for the first time, showing important applications in developing novel SnTe based devices in the future.

The photodetector based on the ultra-thin SnTe nanofilm exhibited a photoelectric response over a broad spectral range of 400-1050 nm. The responsivity (R) and detectivity (D^*) of the device were 1.71 AW^{-1} and 3.46×10^{11} $cmHz^{1/2}W^{-1}$, respectively, under NIR illumination of 940 nm at an optical power density of 0.2 $mWcm^{-2}$. The device performed significantly better than previously reported SnTe photoconductive devices. If the device is encapsulated, its performance can improve further. Therefore, in this study, we prepared and used sputtered SnTe nanofilms for the development of high-performance broadband photodetectors, which have numerous important application prospects.

Funding. National Key Research and Development Program of China (2019YFB2203404); National Natural Science Foundation of China (11864044).

Disclosures. The authors declare no conflicts of interest.

Data availability. Data underlying the results presented in this paper are not publicly available at this time but may be obtained from the authors upon reasonable request.

References

1. C. L. Li, H. L. Wang, F. Wang, T. F. Li, M. J. Xu, H. Wang, Z. Wang, X. W. Zhan, W. D. Hu, and L. Shen, "Ultrafast and broadband photodetectors based on a perovskite/organic bulk heterojunction for large-dynamic-range imaging," Light Sci Appl **9**(1), 31 (2020).
2. L. Wang, J. S. Jie, Z. B. Shao, Q. Zhang, X. H. Zhang, Y. M. Wang, Z. Sun, and S. T. Lee, "MoS_2/Si Heterojunction with Vertically Standing Layered Structure for Ultrafast, High-Detectivity, Self-Driven Visible–Near Infrared Photodetectors," Adv. Funct. Mater. **25**(19), 2910–2919 (2015).
3. Y. Liu, N. O. Weiss, X. D. Duan, H. C. Cheng, Y. Huang, and X. F. Duan, "Van der Waals Heterostructures and Devices," Nat. Rev. Mater. **1**(9), 16042 (2016).
4. F. K. Wang, L. G. Li, W. J. Huang, L. Li, B. Jin, H. Q. Li, and T. Y. Zhai, "Submillimeter 2D Bi_2Se_3 Flakes toward High-Performance Infrared Photodetection at Optical Communication Wavelength," Adv. Funct. Mater. **28**(33), 1802707 (2018).
5. H. H. Sun, T. Jiang, Y. Y. Zang, X. Zheng, Y. Gong, Y. Yan, Z. J. Xu, Y. Liu, L. Fang, X. A. Cheng, and K. He, "Broadband ultrafast photovoltaic detectors based on large-scale topological insulator Sb2Te3/STO heterostructures," Nanoscale **9**(27), 9325–9332 (2017).
6. J. D. Yao and G. W. Yang, "Flexible and High-Performance All-2D Photodetector for Wearable Devices," Small **14**(21), 1704524 (2018).
7. B. A. Assaf, F. Katmis, P. Wei, B. Satpati, Z. Zhang, S. P. Bennett, V. G. Harris, J. S. Moodera, and D. Heiman, "Quantum coherent transport in SnTe topological crystalline insulator thin films," Appl. Phys. Lett. **105**(10), 102108 (2014).
8. S. H. Gu, K. Ding, J. Pan, Z. B. Shao, J. Mao, X. J. Zhang, and J. S. Jie, "Self-Driven, Broadband and Ultrafast Photovoltaic Detectors Based on Topological Crystalline Insulator SnTe/Si Heterostructures," J. Mater. Chem. A **5**(22), 11171–11178 (2017).
9. T. Jiang, Y. Y. Zang, H. H. Sun, X. Zheng, Y. Liu, Y. Gong, L. Fang, X. A. Cheng, and K. He, "Broadband High-Responsivity Photodetectors Based on Large-Scale Topological Crystalline Insulator SnTe Ultrathin Film Grown by Molecular Beam Epitaxy," Adv. Opt. Mater. **5**(5), 1600727 (2017).
10. J. L. Liu, X. Li, H. Wang, G. Yuan, A. Suvorova, S. Gain, Y. L. Ren, and W. Lei, "Ultrathin High-Quality SnTe Nanoplates for Fabricating Flexible Near-Infrared Photodetectors," ACS Appl. Mater. Interfaces **12**(28), 31810–31822 (2020).
11. Y. J. Feng, H. C. Chang, Y. B. Liu, N. Guo, J. K. Liu, L. Xiao, and L. S. Li, "Ultralow dark current infrared photodetector based on SnTe quantum dots beyond 2 μm at room temperature," Nanotechnology **32**(19), 195602 (2021).
12. R. Moshwan, L. Yang, J. Zou, and Z. G. Chen, "Eco-Friendly SnTe Thermoelectric Materials: Progress and Future Challenges," Adv. Funct. Mater. **27**(43), 1703278 (2017).

Optics EXPRESS

13. P. Tanwar, A. K. Panwar, S. Singh, and A. K. Srivastava, "Comparison of Structural, Electrical and Thermoelectric Properties of Vacuum Evaporated SnTe Films of Varied Thickness," J. Nanosci," j nanosci nanotechnol **20**(6), 3879–3887 (2020).
14. S. N. Masoud, B. Mehdi, and D. Fatemeh, "Simple routes to synthesis and characterization of nanosized tin telluride compounds," Appl. Surf. Sci. **257**(3), 781–785 (2010).
15. S. Sugai, K. Murase, and H. Kawamura, "Observation of soft TO-phonon in SnTe by Raman scattering," Solid State Commun. **23**(2), 127–129 (1977).
16. H. C. Wang, J. Hwang, C. Zhang, T. Wang, W. B. Su, H. Kim, J. Kim, J. Zhai, X. Wang, H. Park, W. Kim, and C. L. Wang, "Enhancement of the thermoelectric performance of bulk SnTe alloys via the synergistic effect of band structure modification and chemical bond softening," J. Mater. Chem. A **5**(27), 14165–14173 (2017).
17. H. Anamul, B. Ananya, V. Rahul Mahavir, S. Indranil, B. Kanishka, and S. Pralay K, "Understanding the Chemical Nature of the Buried Nanostructures in Low Thermal Conductive Sb-Doped SnTe by Variable Energy Photoelectron Spectroscopy," J. Phys. Chem. C **123**(16), 10272–10279 (2019).
18. V. S. Neudachina, T. B. Shatalova, V. I. Shtanov, L. V. Yashina, T. S. Zyubina, M. E. Tamm, and S. P. Kobeleva, "XPS study of SnTe(100) oxidation by molecular oxygen," Surf. Sci. **584**(1), 77–82 (2005).
19. S. Singh, S. Kumar, and R. Venkatesh, "Simultaneous Enhancement in Thermopower and Electrical Conductivity of SnTe-Te Nano Heterostructures," Mater. Lett. **302**, 130414 (2021).
20. Y. C. Zou, Z. G. Chen, F. T. Kong, E. Zhang, J. Drennan, K. Cho, F. X. Xiu, and J. Zou, "Surface-energy engineered Bi-doped SnTe nanoribbons with weak antilocalization effect and linear magnetoresistance," Nanoscale **8**(46), 19383–19389 (2016).
21. R. Adhikari, V. V. Volobuev, B. Faina, G. Springholz, and A. Bonanni, "Ferromagnetic phase transition in topological crystalline insulator thin films: interplay of anomalous Hall angle and magnetic anisotropy," Phys. Rev. B **100**(13), 134422 (2019).
22. X. F. Qian, L. Fu, and J. Li, "Topological crystalline insulator nanomembrane with strain-tunable band gap," Nano Res. **8**(3), 967–979 (2015).
23. X. Gong, M. H. Tong, Y. J. Xia, W. Z. Cai, J. S. Moon, Y. Cao, G. Yu, C. L. Shieh, B. Nilsson, and A. J. Heeger, "High-Detectivity Polymer Photodetectors with Spectral Response from 300 nm to 1450 nm," Science **325**(5948), 1665–1667 (2009).
24. H. B. Zhang, B. Y. Man, and Q. Zhang, "Topological Crystalline Insulator SnTe/Si Vertical Heterostructure Photodetectors for High-Performance Near-Infrared Detection," ACS Appl. Mater. Interfaces **9**(16), 14067–14077 (2017).
25. H. B. Zhang, Z. L. Song, D. Li, Y. C. Xu, J. Li, C. J. Bai, and B. Y. Man, "Near-infrared photodetection based on topological insulator P-N heterojunction of SnTe/Bi_2Se_3," Appl. Surf. Sci. **509**(4), 145290 (2020).
26. J. L. Liu, H. Wang, X. Li, H. Chen, Z. K. Zhang, W. W. Pan, G. Q. Luo, C. L. Yuan, Y. L. Ren, and W. Lei, "Ultrasensitive Flexible Near-Infrared Photodetectors Based on Van Der Waals Bi_2Te_3 Nanoplates," Appl. Surf. Sci. **484**, 542–550 (2019).
27. Q. S. Wang, Y. Wen, F. R. Yao, Y. Huang, Z. X. Wang, M. L. Li, X. Y. Zhan, K. Xu, F. M. Wang, F. Wang, J. Li, K. H. Liu, C. Jiang, F. Q. Liu, and J. He, "BN-Enabled Epitaxy of $Pb_{1-x}Sn_xSe$ Nanoplates on SiO_2/Si for High-Performance Mid-Infrared Detection," Small **11**(40), 5388–5394 (2015).